Journal of Materials Chemistry C

Accepted Manuscript

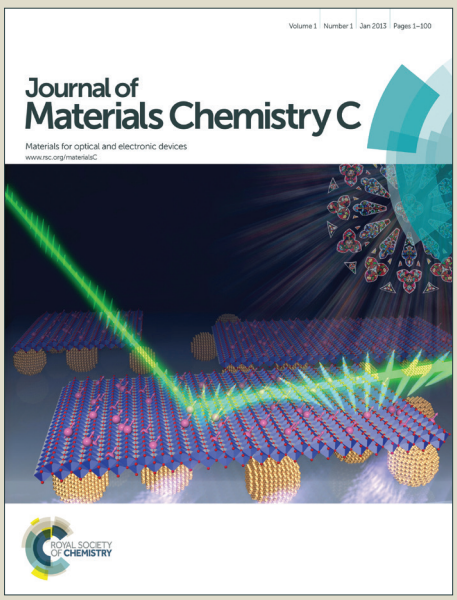

ROYAL SOCIETY OF CHEMISTRY

www.rsc.org/materialsC

Journal Name

ARTICLE

Received 00th January 20xx,

Accepted 00th January 20xx

DOI: 10.1039/x0xx00000x

www.rsc.org/

Enhanced average thermoelectric figure of merit of *n*-type $PbTe_{1-x}I_x$–MgTe

Priyanka Jood,[a] Michihiro Ohta,†,[a] Masaru Kunii,[a] Xiaokai Hu,[a] Hirotaka Nishiate,[a] Atsushi Yamamoto,[a] and Mercouri G. Kanatzidis[b,c]

The thermoelectric properties of sintered samples of *n*-type $PbTe_xI_{1-x}$–*y*MgTe (x = 0.0012–0.006; y = 0 and 1 %) were investigated over the temperature range of 300 K to 873 K. Scanning electron microscopy revealed two different length scales of grains in samples with higher I and MgTe contents, while a homogenous microstructure for samples with lower dopant content. Transmission electron microscopy revealed ubiquitous spherical nanoprecipitates in $PbTe_xI_{1-x}$ with MgTe and nanoscale disk like precipitates in both, $Pb_xTe_{1-x}I_x$ with and without MgTe. The nanostructured PbTe showed higher Seebeck coefficients than expected values. We also observed a slower rate of increase in the electrical resistivity with rising temperature in $PbTe_xI_{1-x}$–*y*MgTe below ~550 K, leading to higher thermoelectric power factor. The nanostructures and mixed microstructures scatter phonons, reducing the lattice thermal conductivity as low as 0.4 W K^{-1} m^{-1} at 600 K. A high *ZT* of 1.2 at 700 K was achieved as well as a high average *ZT* of 0.8 was observed in $PbTe_{0.996}I_{0.004}$–1mol% MgTe for cold-side temperature of 303 K and hot-side temperature of 873 K.

Introduction

The energy utilization efficiency must be enhanced to reduce greenhouse-gas emissions and improve energy management and sustainability. Solid-state devices based on thermoelectrics directly convert waste heat to electrical energy without hazardous emissions, and therefore this technology is considered as a sustainable clean energy source. The conversion efficiency of a thermoelectric device is determined by material's dimensionless thermoelectric figure of merit, $ZT = (S^2/\rho\kappa_{total})T$, where S, ρ, κ_{total}, and T are the Seebeck coefficient, electrical resistivity, total thermal conductivity, and absolute temperature, respectively. The κ_{total} arises from charge carriers transporting heat (*i.e.*, electronic thermal conductivity, κ_{el}) and phonons travelling through the lattice (*i.e.*, lattice thermal conductivity, κ_{lat}); therefore, $\kappa_{total} = \kappa_{el} + \kappa_{lat}$, where κ_{el} can be estimated using the Wiedemann-Franz law: $\kappa_{el} = LT/\rho$, where L is the Lorenz number. To obtain high *ZT*, the thermoelectric power factor (S^2/ρ) must be enhanced and κ_{total} must be reduced. The most successful approach to enhance *ZT* by reducing lattice thermal conductivity is to embed suitable nanoscale precipitates in bulk materials that effectively scatter phonons[1–11]. Alternate approach is to improve the power factor through carrier concentration optimization[12,13], band structure engineering[14,15], electron energy barrier filtering[16,17], and quantum confinement[18].

Till date, PbTe-based bulk materials have the best thermoelectric performance in the intermediate temperature range (500 K-900 K)[8–10,19–24]. Panoscopic approach[10,11,23,25] has proven very successful in enhancing *ZT* of *p*-type PbTe to values as high as ~2.2 at 915 K. It involves phonon scattering at all relevant length scales by introducing multi-scale defects in the system. For instance, atomic scale lattice disorders and endotaxially embedded nanoprecipitates scatter short to mid wavelength phonons and meso-structuring through sintering effectively scatters the long wavelength phonons[10,22]. Group II tellurides (MgTe, CaTe, SrTe, and BaTe)[9,10,20,23] and group IIB tellurides (CdTe and HgTe)[22] have been used for nanostructuring in *p*-type PbTe. The endotaxial crystallographic alignment of the nanoprecipitates with the PbTe lattice prevents the carrier mobility to be affected, maintaining the power factor. Among all the above mentioned nanoprecipitates, MgTe nanostructuring[9,23] is particularly interesting as it is found to have a solid state solubility (under 3 mol%)[7,26] in PbTe. MgTe decreases the energy difference between the light and heavy valence bands (L and Σ bands) enhancing the Seebeck coefficient in *p*-type samples. Additionally, the resulting increased bandgap suppresses the bipolar thermal conductivity, reducing κ_{total} further.

[a] *Research Institute for Energy Conservation, National Institute of Advanced Industrial Science and Technology (AIST), Tsukuba, Ibaraki 305-8568.*
[b] *Department of Chemistry, Northwestern University, Evanston, Illinois 60208, USA*
[c] *Materials Science Division, Argonne National Laboratory, Argonne, Illinois 60439,USA.*
† Corresponding Author E-mail: ohta.michihiro@aist.go.jp.
Electronic Supplementary Information (ESI) available: [Heat capacity, thermal diffusivity, zoom-in powder X-ray diffraction patterns, calculated Lorenz number, electron mobility, carrier concentration, density]. See DOI: 10.1039/x0xx00000x

The *n*-type PbTe, however, has not yet benefitted from the latest developments of panoscopic approach. One reason for this is that the *n*-type doping is essentially single band transport. Until recently, the commonly stated peak *ZT* for *n*-type PbTe had been about unity[27,28]. The recent reports on reassessment of thermal transport properties[19], exploration of resonance levels[29,30] and optimization of carrier concentration[13,31] have provided a renewed interest in *n*-type PbTe based materials. Furthermore, for thermoelectric module development, both *p* and *n*-type legs are required, preferably of the same material to benefit from similar properties, such as thermal expansion. This motivated us to investigate the effects of MgTe addition on the thermoelectric properties of PbI_2 doped *n*-type PbTe. MgTe addition proved critical in enhancing the average *ZT* of *n*-type PbTe. Here, we also provide an account of the influence of dopant atoms (I and MgTe) on the nano/micro structure of PbTe and their correlation with the thermoelectric properties.

Experimental Section

Synthesis and Sintering

Elemental lead (Pb; 99.9999%, Osaka Asahi Metal MFG), elemental tellurium (Te; 99.9999%, Osaka Asahi Metal MFG), elemental magnesium (Mg; 99.999%, Osaka Asahi Metal MFG), and lead iodide (PbI_2; 99.999%, Sigma-Aldrich) were used as starting materials without further purification. Ingots (~12 g) with nominal compositions of $PbTe_{1-x}I_x$–*y*MgTe (x= 0.0012–0.012; y= 0–2 mol%) were synthesized by mixing appropriate ratios of starting materials of Pb, Te, Mg, and PbI_2 in carbon-coated quartz tubes under an N_2-filled glove box. For example, 7.378 g of Pb, 4.580 g of Te, 0.009 g of Mg, and 0.033 g of PbI_2 were used to prepare 12 g of $PbTe_{0.996}I_{0.004}$–1% MgTe. The tubes were evacuated to 7×10^{-3} Pa and then sealed. They were heated to 1323 K at a rate of 1.47 K min^{-1} and then held at 1323 K for 5 h. The samples were then cooled to 1023 K at a rate of 8.5 K min^{-1} and held for 4 h, and ultimately cooled to room temperature over 12 h.

The prepared ingots were crushed into powders and were placed into 10-mm- or 15-mm-diameter graphite dies which were then inserted into the sintering equipment (SPS-515S, Fuji Electronic Industrial) and heated at 10 K min^{-1}. Sintering was performed at 773 K for 1 h under 30 MPa uniaxial pressure in vacuum (7×10^{-3} Pa) and subsequently cooled at 20 K min^{-1} to prepare sintered compacts. The disks of ~15 mm diameter × ~3 mm thickness were cut into bars for electrical transport measurements. The disks of ~10 mm diameter ×~2 mm thickness were used for thermal transport measurements.

Powder X-ray Diffraction, Scanning Electron Microscopy and Transmission Electron Microscopy

The crystal structure of the synthetic powders and sintered compacts were examined using X-ray diffractometry (XRD; Miniflex, Rigaku) with Cu Kα radiation over the 2ϑ range 20–80°. The microstructures of the sintered compacts were observed using scanning electron microscopy (SEM; JSM-6610LV, 20 kV, JEOL).

Transmission electron microscopy (TEM) and electron diffraction (ED) studies were performed using FEI Tecnai Osiris microscope operated at 200 kV. The TEM samples were prepared by polishing and Ar ion-milling.

Electrical Transport Measurements

The Seebeck coefficient and electrical resistivity of the sintered compacts were simultaneously measured using temperature-differential and four-probe methods, respectively, (ZEM-3, ULVAC-RIKO) under a He atmosphere in the temperature range of 300 K to 900 K. The bars used for the measurements typically were ~3 mm ×~2 mm × ~10 mm. The heating and cooling cycles provide reproducible Seebeck coefficient and electrical resistivity for all the sintered compacts. The uncertainty of the Seebeck coefficient and electrical conductivity measurements is ~5%.

The Hall coefficient of the sintered compacts was measured using a homemade system under a magnetic field from 0 T to 2.3 T at room temperature. The samples typically were ~5 mm ×~5 mm × ~0.4 mm. In-rich In-Ga paste was used to attach Cu contact wires to the samples. The room-temperature electron mobility (μ) and carrier concentration (*n*) are given in Table S1 in the Supplementary Information.

Thermal Transport Measurements

The total thermal conductivity (κ_{total}) was calculated using the density (*d*) of the sintered compacts, the thermal diffusivity (*D*), the heat capacity (C_P) and the equation $\kappa_{total} = DC_Pd$. The thermal diffusivity was directly measured and the heat capacity was indirectly derived using a standard sample (Pyroceram 9606) and laser flash method (LFA 457 MicroFlash, Netzsch) over the temperature range of 300 K to 900 K under Ar flowing at 100 mL min^{-1}. The samples used for the measurements were typical ~10-mm-diameter, ~2-mm-thick coins. The heating and cooling cycles enable the repeatable thermal diffusivity for all the sintered compacts. The thermal diffusivity and heat capacity data are provided in Fig. S1 in the Supplementary Information. The density of the sintered compacts was determined using Gas pycnometer method (Accu Pyc 11 1340, Micromeritics). All samples showed a density >98% of the theoretical density (Table S2 in the Supplementary Information).

The uncertainty of the thermal conductivity is estimated to be within 8%, taking into account the uncertainties for *D*, C_P, and *d*. The combined uncertainty for all measurements involved in the calculation of *ZT* is around 12%. Higher MgTe content, for example *y*= 2 mol%, in *n*-type PbTe yields poor thermoelectric performance (Fig. S2 of Supplementary information). Therefore, in this study we focused only on the thermoelectric properties of $PbTe_{1-x}I_x$–*y*MgTe (x= 0.0012–0.006; y= 0–1 mol%).

Results and discussion

We obtained scanning electron microscopy (SEM) images to determine the morphological differences among the samples (Fig. 1). The grain size of $PbTe_{0.9972}I_{0.0028}$ was nearly homogenous, with an average of ~30 μm. Interestingly, for $PbTe_{0.9972}I_{0.0028}$ sample containing 1% MgTe, two different length scales of grains were observed to co-exist; one set with average grain size ~30 μm and another with grain size between 0.5–2 μm. Similar morphology was observed for all the higher doped samples (x > 0.0028) with and without MgTe. Higher dopant concentration probably promotes the brittleness of PbTe which gives rise to a mixed microstructure.

We performed high resolution transmission electron microscopy (TEM) on sintered samples to analyse the nanoscale structure of *n*-type PbTe (with and without MgTe). Fig. 2a shows a mid-magnification image of $PbTe_{0.996}I_{0.004}$ along the [001] zone axis, where many nanoscale disk-shaped imperfections of 3-5 nm in size can be observed. Bright lobe-like regions representing lattice strain fields can be seen on each side of the disks. Lattice strain contrast images are also presented in Fig. 2b, recorded along the [111] zone axis. These disk shaped defects in PbTe (possibly 1-2 atomic layers thick[24]) have been observed by many authors in the past and were interpreted differently in each case, such as Te vacancies[4], Pb vacancies[32] or Pb nanoprecipitates[10,19,24]. The results depend on various factors, such as sample preparation techniques, Pb/Te atomic ratio, role of the dopant and its concentration in PbTe. It is difficult to characterize these defects through energy-dispersive X-ray spectroscopy (EDS) due to their small size. We also found large Pb precipitates (average size ~5 μm) in the sample identified by scanning transmission electron microscopy (STEM; Fig. 2c) and EDS mapping (Fig. 2d and 2e).

The sample of $PbTe_{0.996}I_{0.004}$ with 1% MgTe was also investigated using high resolution TEM (Fig. 3). We found two different kinds of nanoprecipitates in this sample, pseudo spherical and disk shaped. Fig. 3a shows a high magnification TEM image of MgTe induced nanocrystal with ~5nm diameter embedded endotaxially in the PbTe matrix and having a pseudo-spherical shape. The inset of Fig. 3c shows an electron diffraction pattern with an aperture including the nanoprecipitates and PbTe matrix. The diffraction pattern does not show any split spots implying that the nanoprecipitates are coherently placed in the matrix. The mid and low magnification image shows mixed nanoscale imperfections (Fig. 3b and 3c). The ones with spherical dark contrast and size distribution of 2-10 nm are MgTe induced nanoprecipitates (also observed in the STEM image in Fig. 3d) and the others with slightly bigger disk-like dark contrasts are lattice strains produced by the disk shaped nanoprecipitates which were also observed for MgTe-free sample.

Powder X-ray diffraction (XRD) patterns of the $PbTe_{1-x}I_x$–MgTe samples are shown in Fig. 4. The patterns are consistent with the cubic NaCl-type PbTe structure, with no MgTe or other secondary phases observable within the detection limits of our XRD. However, for $PbTe_{0.9972}I_{0.0028}$–2% MgTe signs of peak splitting can be observed suggesting the presence of MgTe secondary phase (Fig. S3). We estimated the lattice parameters of PbTe doped with PbI_2 as well as MgTe containing PbTe doped with PbI_2 from their powder X-ray diffraction patterns. As shown in Fig. 4b, the lattice parameter, a of our $PbTe_{1-x}I_x$ samples deviates considerably from the trend of a solid solution where simply I^{1-} (~ 2.20 Å for six coordination) takes place of Te^{2-} (~ 2.21 Å for six coordination). This deviation from Vegard's law is caused by the strains induced by the disk shaped nanoprecipitates present in the samples, as described above. However, the concentration of nanoprecipitates may only increase to a certain level after which they saturate**,** as a consequence of which we see a decrease in a for x > 0.0028.

Fig. 4c shows the trend for the lattice parameter, a for 1 and 2 % MgTe containing $PbTe_{1-x}I_x$ (x= 0.0028, 0.004, and 0.006). For all samples, the addition of MgTe decreases a because the Mg^{2+} ion with six coordination (~0.86 Å) is smaller than Pb^{2+} (~1.19 Å). Furthermore, the MgTe insertion appears to cause the expulsion of dopant atoms (I) from the PbTe lattice[7], which can also reduce a. This is supported by the electrical measurements discussed below which show a decrease in room temperature electron concentration with MgTe insertion. Similar results were obtained for *p*-type Na_2Te doped PbTe, where CaTe or MgTe additions causes a significant deviation of a from Vegard's law[9,20.]

Fig. 5a presents the Seebeck coefficient (S) as a function of temperature for $PbTe_{1-x}I_x$–MgTe ($0.0012 \le x \le 0.006$; y = 0 and 1 mol%) samples. The thermoelectric power response is negative in agreement with the Hall measurements (Table S1 in the Supplementary Information) confirming *n*-type conductivity. The S follows almost linear temperature dependence and the room temperature S values are −107, −107, −84, −92, −56, −91, −37, −48 μVK^{-1} for x = 0.0012, x = 0.0012: y = 1, x = 0.0028, x = 0.0028: y = 1, x = 0.004, x = 0.004: y = 1, x = 0.006, x = 0.006: y = 1, respectively. The S values for respective MgTe containing samples are higher, except for x = 0.0012 sample, due to their lower carrier concentrations (n) and implies that MgTe provides further tuning of the n. The x = 0.0012 sample already has a very low I concentration which could be a reason why the MgTe content has low or no effect on Iodine solubility in this sample.

We compared the observed S as a function of carrier concentration with those calculated from a Pisarenko plot using an effective mass m^*=0.25 m_0 (m_0 is the free electron mass) for *n*-type PbTe (Fig. 5b). This comparison is often made to observe any deviation from the standard acoustic phonon scattering of carriers, or the single band approximation and to analyse the possibility of resonance levels[14,23,33]. Our data largely follow the theoretical Pisarenko line with small enhancement seen especially for lower dopant samples. The small grain size, residual strain due to nanostructuring and the presence of dislocations can provide small S enhancements by altering the scattering parameter[33-37]. Furthermore, Pb precipitates in PbTe system are also known to provide S enhancement through an increase in the energy dependence of relaxation time[38].

The temperature dependence of electrical resistivity (ρ) of $PbTe_{1-x}I_x$–*y*MgTe ($0.0012 \leq x \leq 0.006$; y= 0 and 1 mol%), is shown in Fig. 6a. For all samples except $PbTe_{0.9988}I_{0.0012}$ and $PbTe_{0.9972}I_{0.0028}$ (which show a slight decrease in ρ from 300K to 450 K), ρ increases monotonically with temperature indicating degenerate doping. The temperature dependence of resistivity ρ follows a power law $\rho^{-1} \sim T^{-\delta}$ where the exponent δ is ~2.5 in the range of 500 K- 700 K irrespective of MgTe inclusion, which is consistent with *n*-type degenerate PbTe[31] (Fig. S4 of Supplementary information). However, in the temperature range of 300K to 550 K, the exponent δ for PbI_2 doped PbTe with MgTe are smaller than without MgTe. For instance, δ is −1.6 and −1.3 for $PbTe_{0.996}I_{0.004}$ and $PbTe_{0.996}I_{0.004}$–1% MgTe, respectively. The slower rate of increase in resistivity due to MgTe insertion could be a consequence of increase in *n* due to increasing solubility of I into the PbTe matrix with rising temperature.

Fig. 6b, shows the room temperature *n* of our PbI_2 doped PbTe compared to the calculated values, assuming each doped I atom releases one electron into the conduction band. In our case, the *n* for almost all doping levels lies slightly below the expected values, suggesting limited solubility of PbI_2 in the PbTe. Furthermore, a decrease in *n* due to MgTe incorporation is seen for all I doping levels, implying that even a small concentration of MgTe further lowers the solubility of I in the PbTe lattice. For instance, the *n* of $PbTe_{0.996}I_{0.004}$ is 4.05 $\times 10^{19}$ cm^{-3}, whereas with 1% MgTe content in $PbTe_{0.996}I_{0.004}$, *n* is lowered to 2.23 $\times 10^{19}$ cm^{-3} (Table S1 in the Supplementary information). A similar result was obtained for *p*-type PbTe, where MgTe insertion was found to have a detrimental effect on Na solubility, but for a much higher MgTe concentration (≥ 3mol%)[9]. However, with rise in temperature the solubility of I in the PbTe–MgTe shows a larger improvement compared to the MgTe-free PbTe, as suggested above by the resistivity power low.

The room temperature mobility versus carrier concentration are shown in Fig. 6c and compared with few earlier reports[19,39]. The dashed line represents the expected trend for acoustic phonon scattering[24]. In our case, a large deviation from the expected values is seen for lower doping levels, especially for $x = 0.0028$. This is due to the carrier scattering from the strong strains caused by the nanoprecipitates.

The corresponding temperature dependent power factor, S^2/ρ of the $PbTe_{1-x}I_x$–*y*MgTe ($0.0012 \leq x \leq 0.006$; $y = 0$ and 1 mol%) are shown in Fig. 6d. The S^2/ρ of all the samples increase, reaches a maximum and then decreases with increasing temperature. MgTe inclusion results in higher S^2/ρ below 550 K for almost all I doping levels used due to the slower increase of ρ and higher *S*. The highest room temperature value measured is ~1.4 × 10^{-3} W K^{-2} m^{-1} for $PbTe_{0.996}I_{0.004}$–1% MgTe, which rises to a maximum (~2.2 × 10^{-3} W K^{-2} m^{-1}) at around 520 K and yields a value of ~1.3 × 10^{-3} W K^{-2} m^{-1} at ~900 K. The $PbTe_{0.996}I_{0.004}$ sample has a smaller low-temperature S^2/ρ compared to the MgTe containing one, but reaches a similar maximum value of ~2.2 × 10^{-3} W K^{-2} m^{-1} at ~620 K before it falls to ~1.6 × 10^{-3} W K^{-2} m^{-1} at ~900 K.

Fig. 7a and 7b show the total (κ_{total}) and lattice thermal conductivity (κ_{lat}) data as a function of temperature for all the compositions studied, respectively. The κ_{total} increases with increasing I concentration due to the increased electronic thermal conductivity (κ_{el}) contribution. The κ_{el} was estimated using the Wiedemann-Franz law: $\kappa_{el} = LT/\rho$, where *L* is the Lorenz number. The Lorenz number for $PbTe_{1-x}I_x$–*y*MgTe are shown in Fig. S5 in the Supplementary information. The room temperature κ_{lat} of $x = 0.0012$ and $x = 0.0028$ (~2.8 and ~2.9 W K^{-1} m^{-1}, respectively) are the highest among all samples. MgTe included samples for lower I doping levels have about 40% smaller κ_{lat}, ~1.9 and ~1.7 W K^{-1} m^{-1} for $x = 0.0012$–1% MgTe and $x = 0.0028$–1% MgTe, respectively. In higher I doping levels, the κ_{lat} is even more reduced. For example, $x = 0.004$ and $x = 0.005$ have κ_{lat} ~1.5 W K^{-1} m^{-1} at 300 K which reduces to ~0.4 W K^{-1} m^{-1} at ~600 K and increases again to ~ 0.7 W K^{-1} m^{-1} at 900 K. This is mainly due to the nanoprecipitates and mixed microstructure (comprising of coarse and fine grains) which are very effective in the scattering of long and mid wavelength phonons, respectively[36,40,41]. The upturn in the plot of κ_{lat} as a function of temperature above 600 K is due to the bipolar contribution to the thermal conductivity by thermally generated carriers[27].

The thermoelectric figure of merit (*ZT*) values of $PbTe_{1-x}I_x$–*y*MgTe ($0.0012 \leq x \leq 0.006$; $y = 0$ and 1 mol%) are shown in Fig. 8a and the average *ZT* values of our two best samples, $PbTe_{0.996}I_{0.004}$ and $PbTe_{0.996}I_{0.004}$–1% MgTe are shown in Fig. 8b. The highest *ZT* value obtained is ~1.2 for $PbTe_{0.996}I_{0.004}$ and $PbTe_{0.996}I_{0.004}$–1% MgTe at 800 K and 700 K, respectively. In terms of practical applications, the efficiency of a thermoelectric device is based on the average *ZT* of the material rather than the maximum *ZT*. Therefore, it is critical to enhance the average *ZT* over the whole temperature range of operation[12,24]. The average *ZT* of $PbTe_{0.996}I_{0.004}$–1% MgTe is higher in the entire temperature range with a value of ~0.8 at hot-side temperature of 873 K and cold-side temperature of 303 K. The higher average *ZT* for MgTe added sample is attributed to its low κ_{total} in the entire temperature range and higher S^2/ρ at low temperatures (300 -550 K) due to the slow increase of ρ and higher *S*.

Conclusions

This work reveals that the thermoelectric properties of *n*-type PbTe can benefit from MgTe addition. Mixed microstructure was found in samples with higher I and MgTe content which is effective in reducing the lattice thermal conductivity. Two different kinds of nanoprecipitates (spherical and disk shaped) were found in $PbTe_{1-x}I_x$ with MgTe and only disk shaped precipitates were observed for MgTe-free $PbTe_{1-x}I_x$. The strong strain caused by the nanostructures leads to a high Seebeck coefficient and low lattice thermal conductivity. MgTe addition results in a slow rate of increase in electrical resistivity through increased solubility of I and gives rise to higher thermoelectric power factors in low temperature range of 300 to 550 K. The average thermoelectric figure of merit *ZT* of *n*-type $PbTe_{1-x}I_x$ is successfully enhanced by 13% at hot-side temperature of 873

K and cold-side temperature of 303 K through MgTe inclusion. This study provides high performance *n*-type PbTe, which is a step closer to the development of nanostructured PbTe based thermoelectric devices.

Acknowledgements

The authors express our thanks to Ms. Naoko Fujimoto of AIST for preparing the PbTe-based ingots and sintered compacts and Mr. Noriyuki Saitou and Dr. Noriko Yoshizawa of AIST for operating the transmission electron microscope. This work was supported as part of the Japan-U.S. Cooperation Project for Research and Standardization of Clean Energy Technologies funded by the Ministry of Economy, Trade and Industry (METI). P.J. as an International Research Fellow of the Japan Society for the Promotion of Science acknowledges financial support from JSPS KAKENHI Grant Number 15F15068. At AIST, the work supported by the JSPS KAKENHI Grant Number 25420699. At Northwestern, this work was supported as part of the Revolutionary Materials for Solid State Energy Conversion, an Energy Frontier Research Center funded by the U.S. Department of Energy, Office of Science, and Office of Basic Energy Sciences under Award Number DE-SC0001054.

References

1 K. F. Hsu, S. Loo, F. Guo, W. Chen, J. S. Dyck, C. Uher, T. Hogan, E. K. Polychroniadis and M. G. Kanatzidis, *Science*, 2004, **303**, 818.
2 J. R. Sootsman, H. Kong, C. Uher, J. J. D'Angelo, C. I. Wu, T. P. Hogan, T. Caillat and M. G. Kanatzidis, *Angew. Chem., Int. Ed.*, 2008, **47**, 8618.
3 M. G. Kanatzidis, *Chem. Mater.*, 2010, **22**, 648.
4 C. J. Vineis, A. Shakouri, A. Majumdar and M. G. Kanatzidis, *Adv. Mater.*, 2010, **22**, 3970.
5 K. Biswas, J. He, Q. Zhang, G. Wang, C. Uher, V. P. Dravid and M. G. Kanatzidis, *Nat. Chem.*, 2011, **3**, 160.
6 K. Nielsch, J. Bachmann, J. Kimling and H. Böttner, *Adv. Energy Mater.*, 2011, **1**, 713.
7 P. Jood, R. J. Mehta, Y. Zhang, G. Peleckis, X. Wang, R. W. Siegel, T. Borca-Tasciuc, S. X. Dou and G. Ramanath, *Nano Lett.*, 2011, **11**, 4337.
8 S. N. Girard, J. He, X. Zhou, D. Shoemaker, C. M. Jaworski, C. Uher, V. P. Dravid, J. P. Heremans and M. G. Kanatzidis, *J. Am. Chem. Soc.*, 2011, **133**, 16588.
9 M. Ohta, K. Biswas, S. H. Lo, J. He, D. Y. Chung, V. P. Dravid and M. G. Kanatzidis, *Adv. Energy Mater.*, 2012, **2**, 1117.
10 K. Biswas, J. He, I. D. Blum, C. I. Wu, T. P. Hogan, D. N. Seidman, V. P. Dravid and M. G. Kanatzidis, *Nature*, 2012, **489**, 414.
11 L. D. Zhao, V. P. Dravid and M. G. Kanatzidis, *Energy. Environ. Sci.*, 2014, **7**, 251.
12 G. J. Snyder and E. S. Toberer, *Nat. Mater.*, 2008, **7**, 105.
13 Y. Pei, Z. M. Gibbs, A. Gloskovskii, B. Balke, W. G. Zeier and G. J. Snyder, *Adv. Energy Mater.*, 2014, **4**, 1400486.
14 J. P. Heremans, V. Jovovic, E. S. Toberer, A. Saramat, K. Kurosaki, A. Charoenphakdee, S. Yamanaka and G. J. Snyder, *Science*, 2008, **321**, 554.
15 Y. Pei, H. Wang and G. J. Snyder, *Adv. Mater.*, 2012, **24**, 6125.
16 Z. Xiong, X. Chen, X. Huang, S. Bai and L. Chen, *Acta Mater.*, 2010, **58**, 3995.
17 Y. C. Dou, X. Y. Qin, D. Li, L. L. Li, T. H. Zou and Q. Q. Wang, *J. Appl. Phys.*, 2013, **114**, 044906.
18 T. C. Harman, P. J. Taylor, M. P. Walsh and B. E. LaForge, *Science*, 2002, **297**, 2229.
19 A. D. LaLonde, Y. Pei and G. J. Snyder, *Energy Environ. Sci.*, 2011, **4**, 2090.
20 K. Biswas, J. He, G. Wang, S. H. Lo, C. Uher, V. P. Dravid and M. G. Kanatzidis, *Energy Environ. Sci.*, 2011, **4**, 4675.
21 Y. Pei, H. Wang, Z. M. Gibbs, A. D. LaLonde and G. F. Snyder, *NPG Asia Mater.*, 2012, **4**, e28.
22 K. Ahn, K. Biswas, J. He, I. Chung, V. Dravid and M. G. Kanatzidis, *Energy. Environ. Sci.*, 2013, **6**, 1529.
23 L. D. Zhao, H. J. Wu, S. Q. Hao, C. I. Wu, X. Y. Zhou, K. Biswas, J. Q. He, T. P. Hogan, C. Uher, C. Wolverton, V. P. Dravid and M. G. Kanatzidis, *Energy. Environ. Sci.*, 2013, **6**, 3346.
24 H. J. Wu, L. D. Zhao, F. S. Zheng, D. Wu, Y. L. Pei, X. Tong, M. G. Kanatzidis and J. Q. He, *Nat. Commun.*, 2014, **5**.
25 J. He, M. G. Kanatzidis and V. P. Dravid, *Mater. Today*, 2013, **16**, 166.
26 Y. Pei, A. D. LaLonde, N. A. Heinz, X. Shi, S. Iwanaga, H. Wang, L. Chen and G. J. Snyder, *Adv. Mater.*, 2011, **23**, 5674.
27 Y. Ravich, B. Efimova and I. Smirnov, *Semicondicting Lead Chalcogenides*, 1970, Plenum Press.
28 Y. Gelbstein, Z. Dashevsky and M. P. Dariel, *Physica B*, 2005, **363**, 196.
29 K. Ahn, M. K. Han, J. He, J. Androulakis, S. Ballikaya, C. Uher, V. P. Dravid and M. G. Kanatzidis, *J. Am. Chem. Soc.*, 2010, **132**, 5227.
30 P. K. Rawat, B. Paul and P. Banerji, *ACS Appl. Mater. Interfaces*, 2014, **6**, 3995.
31 K. Ahn, C. Li, C. Uher and M. G. Kanatzidis, *Chem. Mater.*, 2009, **21**, 1361.
32 H. Wang, Q. Zhang, B. Yu, H. Wang, W. Liu, G. Chen and Z. Ren, *J. Mater. Res.*, 2011, **26**, 912.
33 K. Kishimoto and T. Koyanagi, *J. Appl. Phys.*, 2002, **92**, 2544.
34 K. Kishimoto, M. Tsukamoto and T. Koyanagi, *J. Appl. Phys.*, 2002, **92**, 5331.
35 J. P. Heremans, C. M. Thrush and D. T. Morelli, *Phys. Rev. B.*, 2004, **70**, 115334.
36 L. D. Zhao, B. P. Zhang, W. S. Liu and J. F. Li, *J. Appl. Phys.*, 2009, **105**, 023704.
37 J. Martin, L. Wang, L. Chen and G. S. Nolas, *Phys. Rev. B.*, 2009, **79**, 115311.
38 J. P. Heremans, C. M. Thrush and D. T. Morelli, *J. Appl. Phys.*, 2005, **98**, 063703.
39 C. Papageorgiou, J. Giapintzakis and T. Kyratsi, *J. Electron. Mater.*, 2013, **42**, 1911.
40 J. F. Li, W. S. Liu, L. D. Zhao and M. Zhou, *NPG Asia Mater.*, 2010, **2**, 152.
41 H. Wang, J. H. Bahk, C. Kang, J. Hwang, K. Kim, J. Kim, P. Burke, J. E. Bowers, A. C. Gossard, A. Shakouri and W. Kim, *Proceedings of the National Academy of Sciences*, 2014, **111**, 10949.

Figure Captions

Fig. 1 Scanning electron microscopy images of (a) $PbTe_{0.9972}I_{0.0028}$, (b) $PbTe_{0.9972}I_{0.0028}$ containing 1 mol% MgTe, (c) $PbTe_{0.996}I_{0.004}$, and (d) $PbTe_{0.996}I_{0.004}$ containing 1 mol% MgTe. A schematic is presented with each image showing the difference in microstructure for clarity. The inset of (b) also shows the high magnification SEM image focussing only on the fine grains.

Fig. 2 Mid-magnification transmission electron microscopy image in (a) [001], (b) [111] zone axis, and (c) scanning transmission electron microscopy image along with the corresponding (d and e) energy-dispersive X-ray spectroscopy mappings of $PbTe_{0.996}I_{0.004}$. The dotted circles indicate the disk shaped nanoprecipitates.

Fig. 3 (a) High, (b) mid, and (c) low magnification transmission electron microscopy images, and (d) scanning transmission electron microscopy image of $PbTe_{0.996}I_{0.004}$ containing 1 mol% MgTe. The arrow and dotted circles indicate the spherical and disk shaped nanoprecipitates, respectively. The inset of (c) shows the electron diffraction pattern including the precipitates and the PbTe matrix.

Fig. 4 (a) Powder X-ray diffraction patterns, (b) lattice parameter versus iodine content in $PbTe_{1-x}I_x$ ($0.0012 \le x \le 0.006$), and (c) lattice parameter versus Mg content in $PbTe_{1-x}I_x$–yMgTe (x= 0.0028, 0.004, 0.006; y= 1 and 2 mol%).

Fig. 5 (a) Temperature dependence of Seebeck coefficient (S), and (b) S as a function of carrier concentration (Pisarenko plot) at 300 K for $PbTe_{1-x}I_x$–yMgTe ($0.0012 \le x \le 0.006$; y = 0 and 1 mol%). (b) also shows the Pisarenko plot of hot pressed bulk $PbTe_{1-x}I_x$[19], nanostructured $PbTe_{1-x}I_x$+1mol%CdTe[29] and small grain sized $PbTe_{1-x}I_x$[33] for comparison.

Fig. 6 (a) Temperature dependence of electrical resistivity (ρ), and (b) room temperature carrier concentrations (n) for all compositions, (c) carrier concentration versus room temperature Hall mobility (μ), and (d) temperature dependence of power factor (S^2/ρ) for $PbTe_{1-x}I_x$–yMgTe ($0.0012 \le x \le 0.006$; y = 0 and 1 mol%). The dashed line in (b) is the expected n for e^- per one iodine atom. Two previously reported works (hot pressed[19] and low temperature synthesized[39] $PbTe_{1-x}I_x$) are also shown for comparison in (c). The dashed line in (c) roughly indicates the expected mobility trend for acoustic phonon scattering.

Fig. 7 Temperature dependence of (a) total thermal conductivity (κ_{total}), and (b) lattice thermal conductivity (κ_{lat}) for $PbTe_{1-x}I_x$–yMgTe ($0.0012 \le x \le 0.006$; y= 0 and 1 mol%).

Fig. 8 (a) Temperature dependence of the thermoelectric figure of merit (ZT) of $PbTe_{1-x}I_x$–yMgTe ($0.0012 \le x \le 0.006$; y = 0 and 1 mol%). (b) Average thermoelectric figure of merit (ZT_{ave}) for the T_H of 400 K to 873 K and T_C= 303 K for $PbTe_{0.996}I_{0.004}$ and $PbTe_{0.996}I_{0.004}$–1 mol% MgTe.

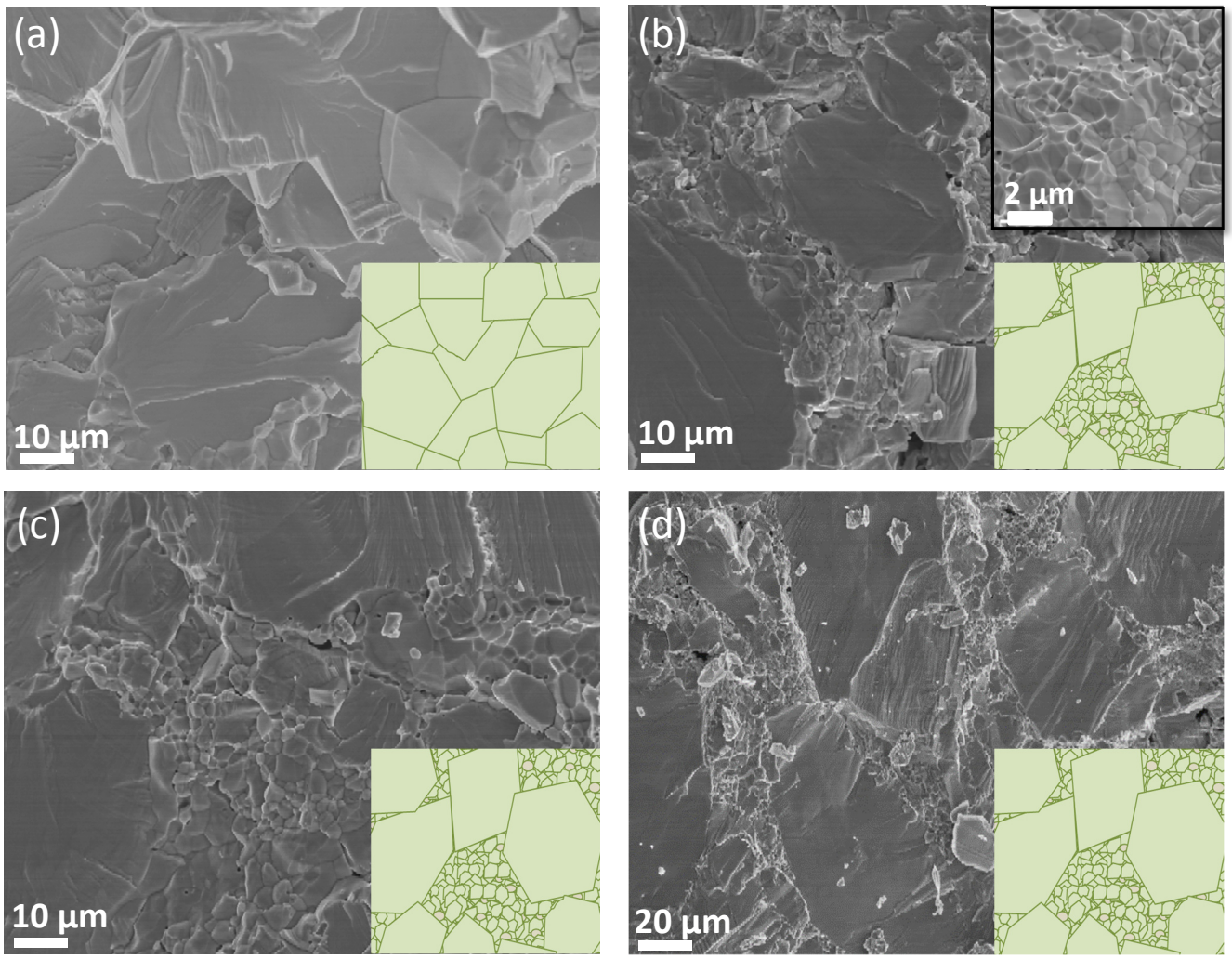

Fig.1

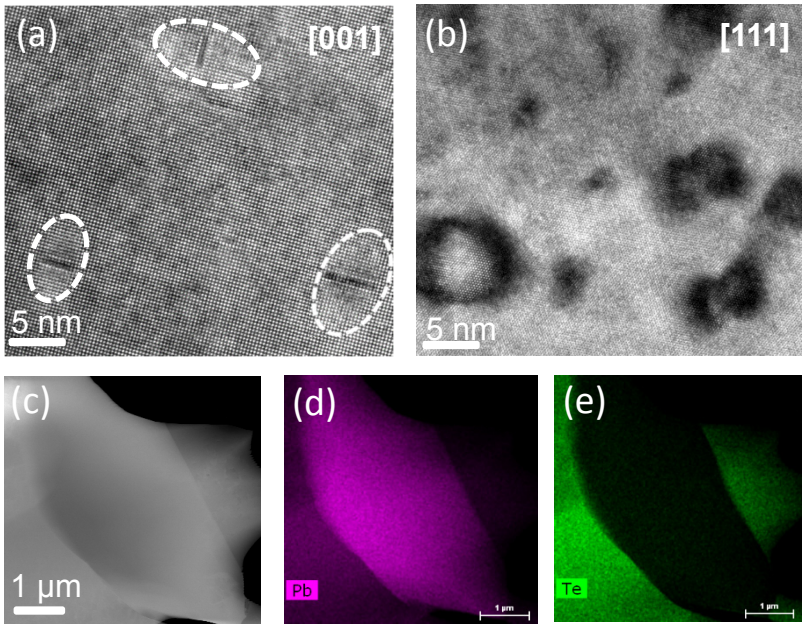

Fig.2

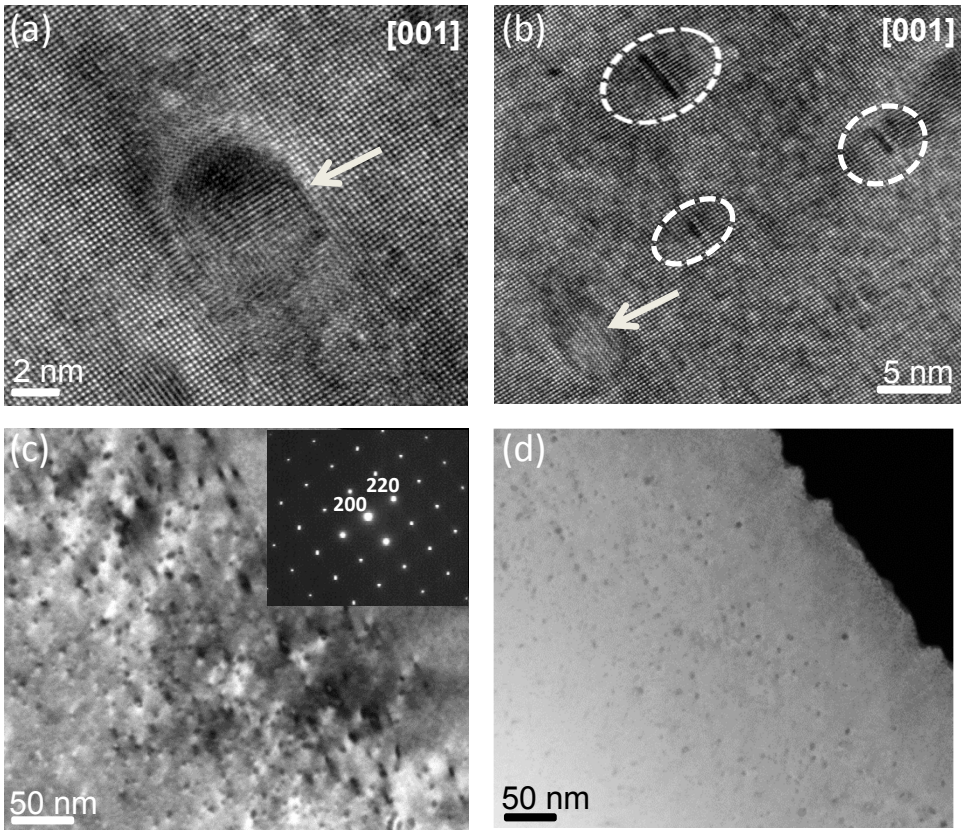

Fig.3

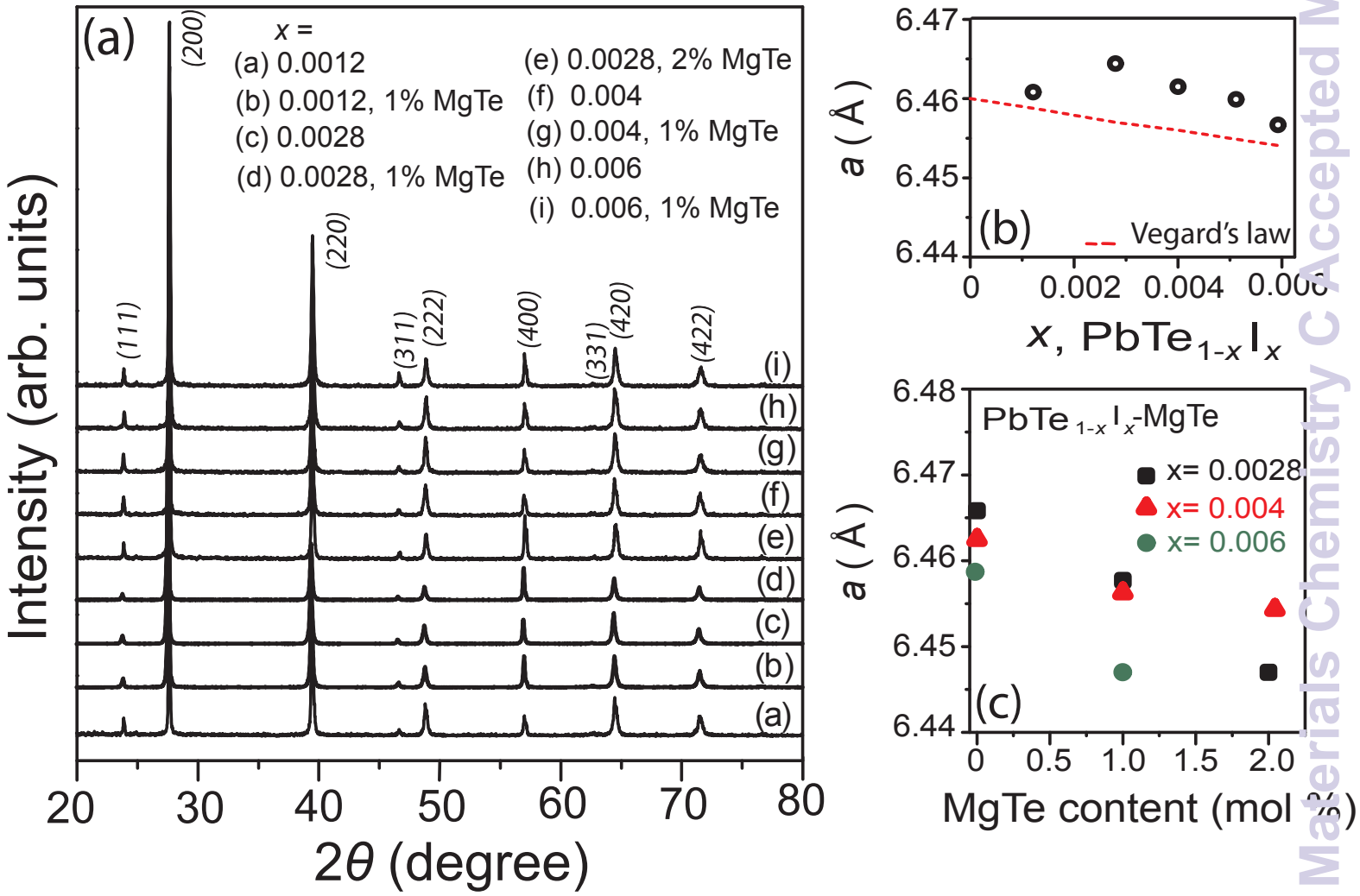

Fig.4

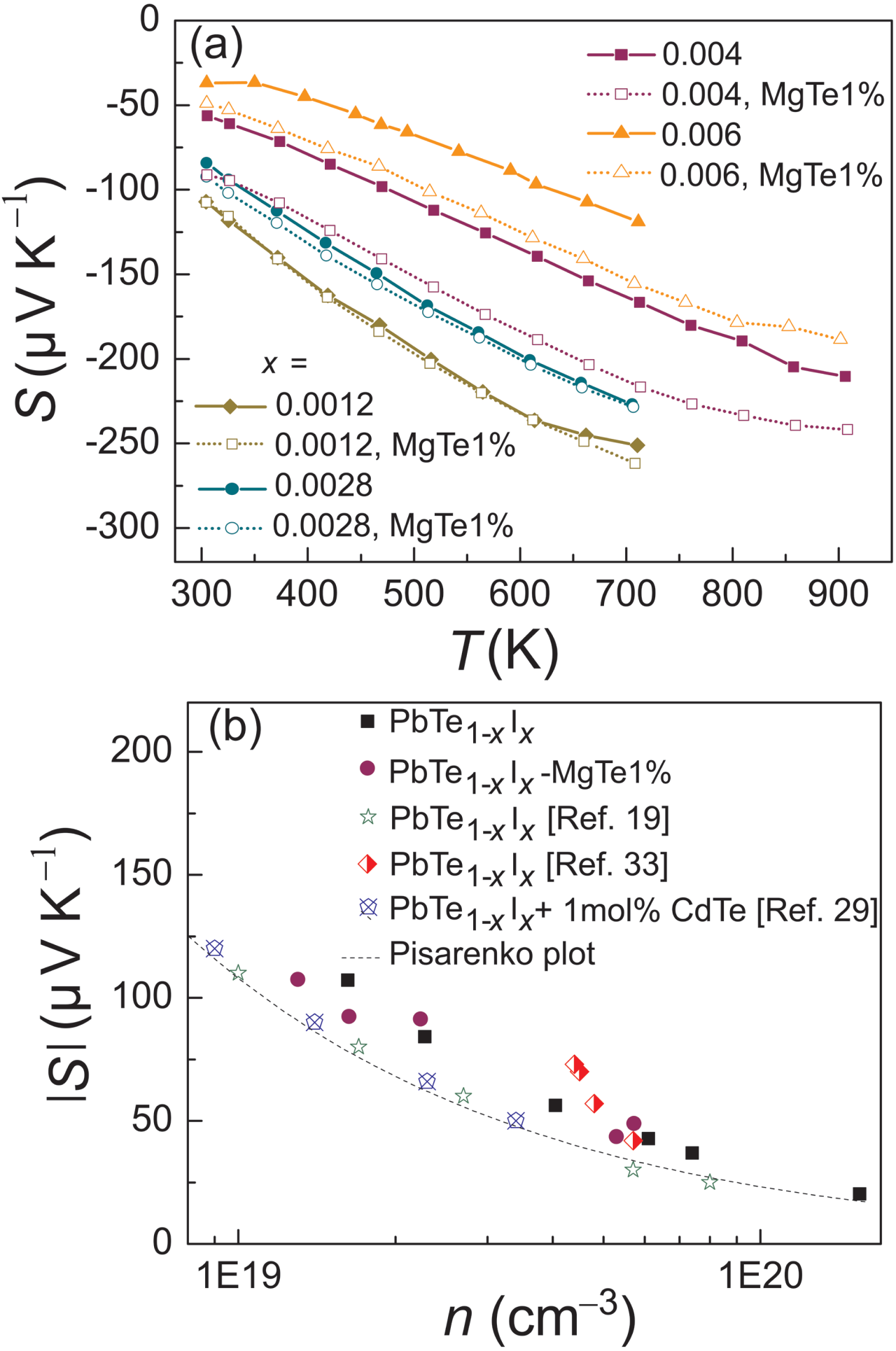

Fig.5

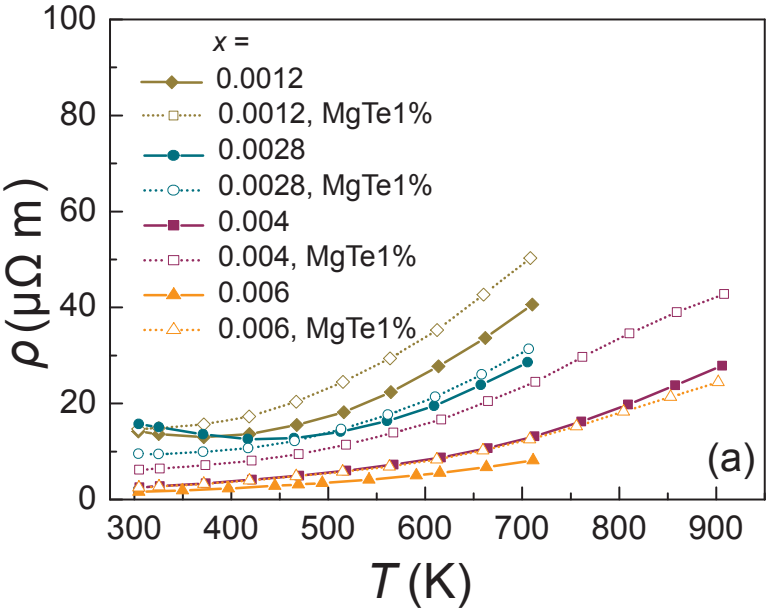

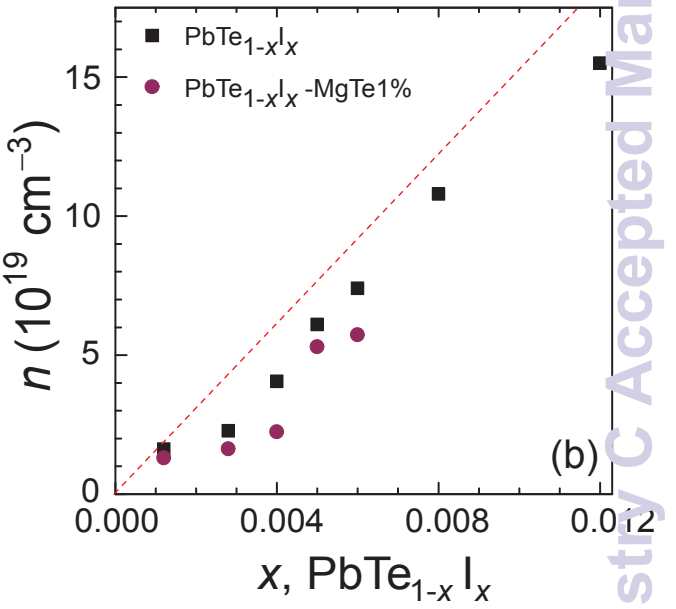

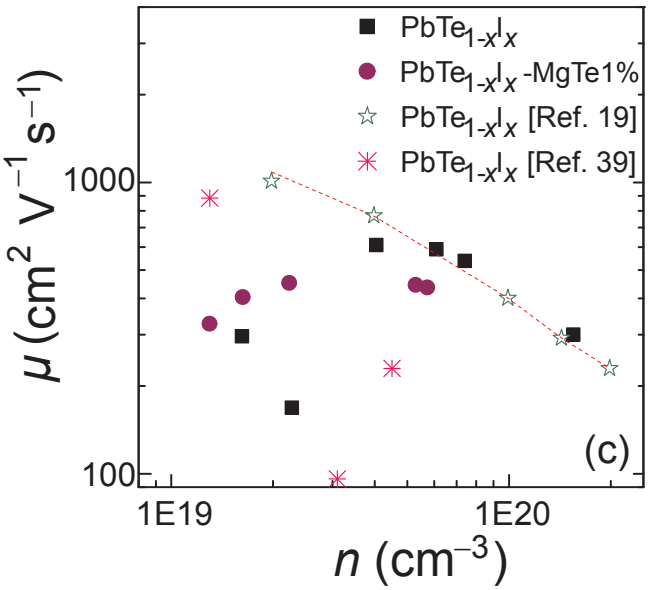

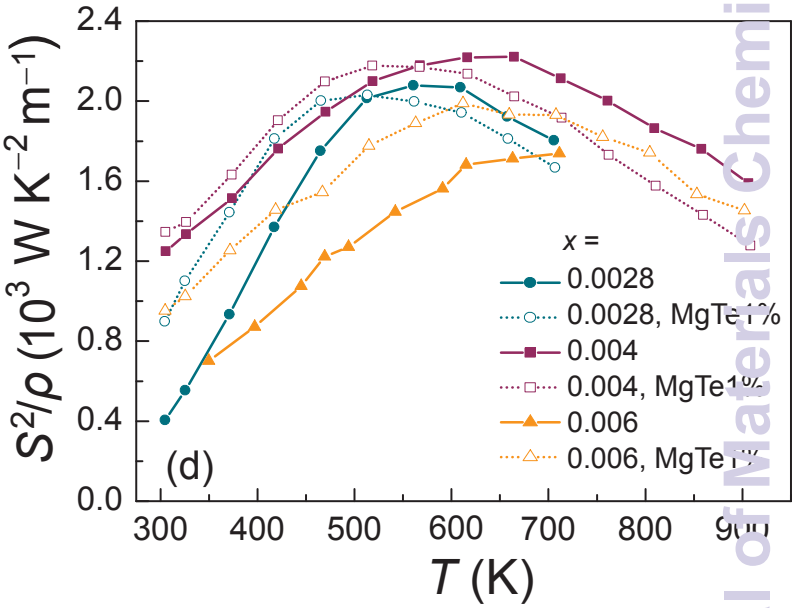

Fig.6

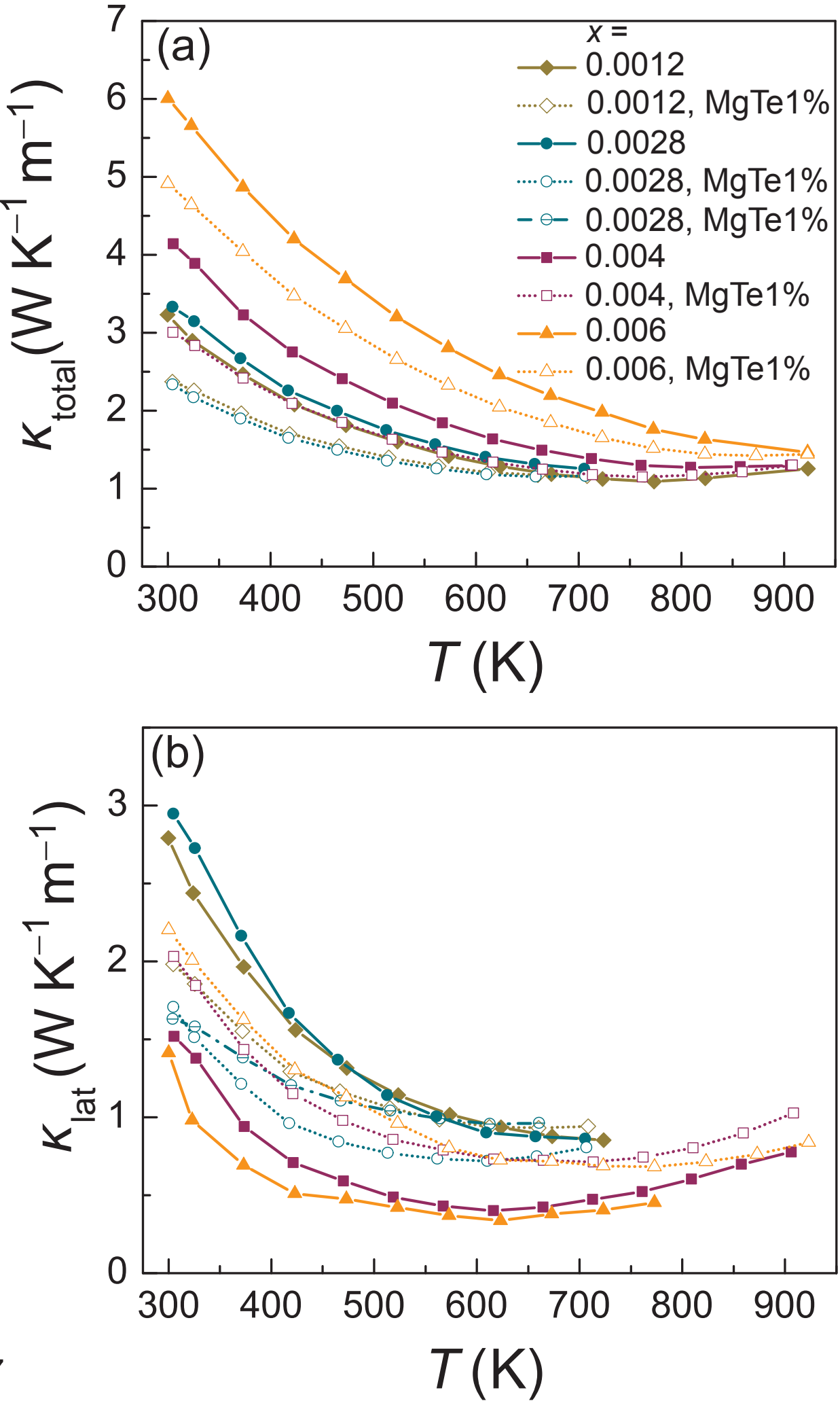

Fig.7

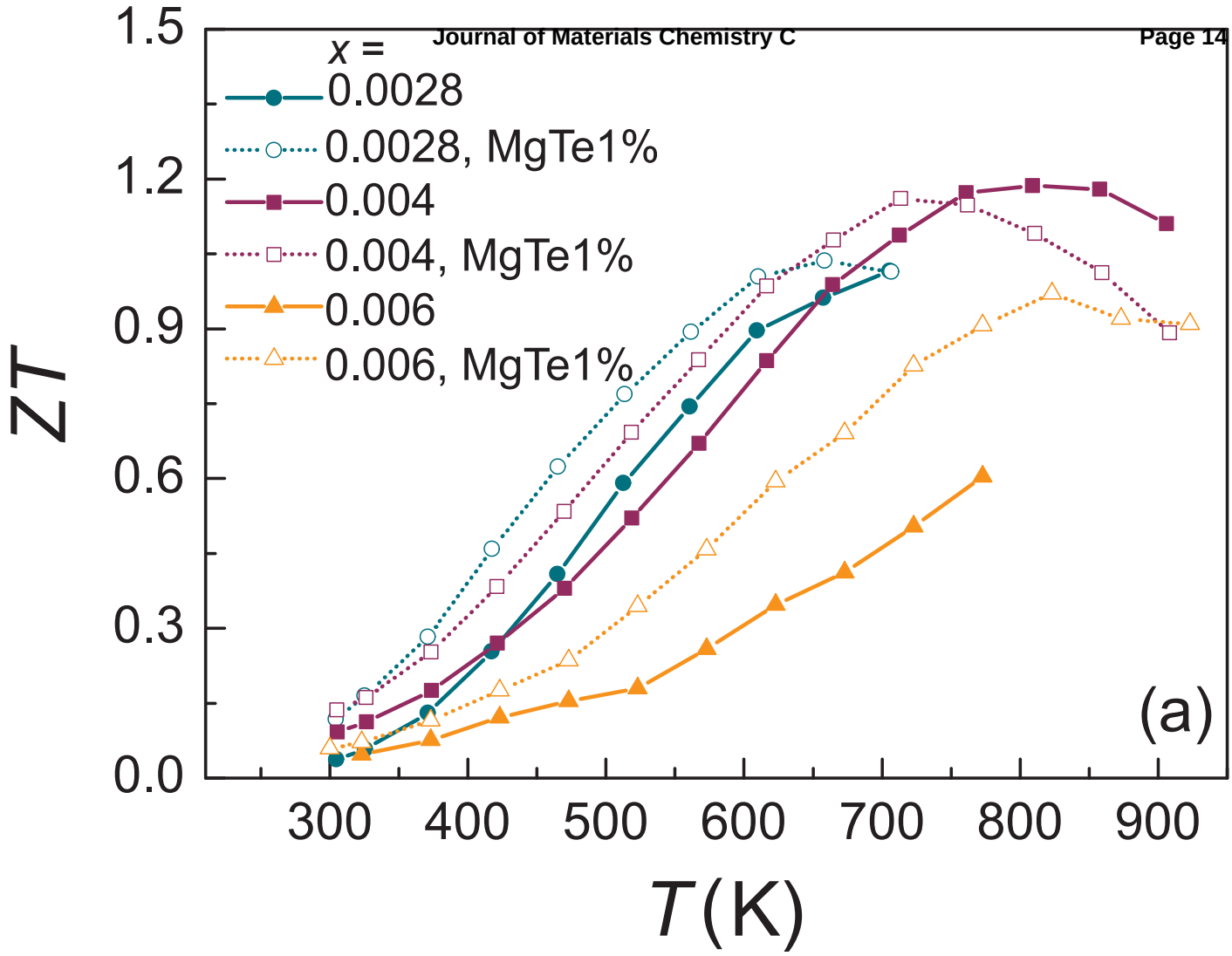

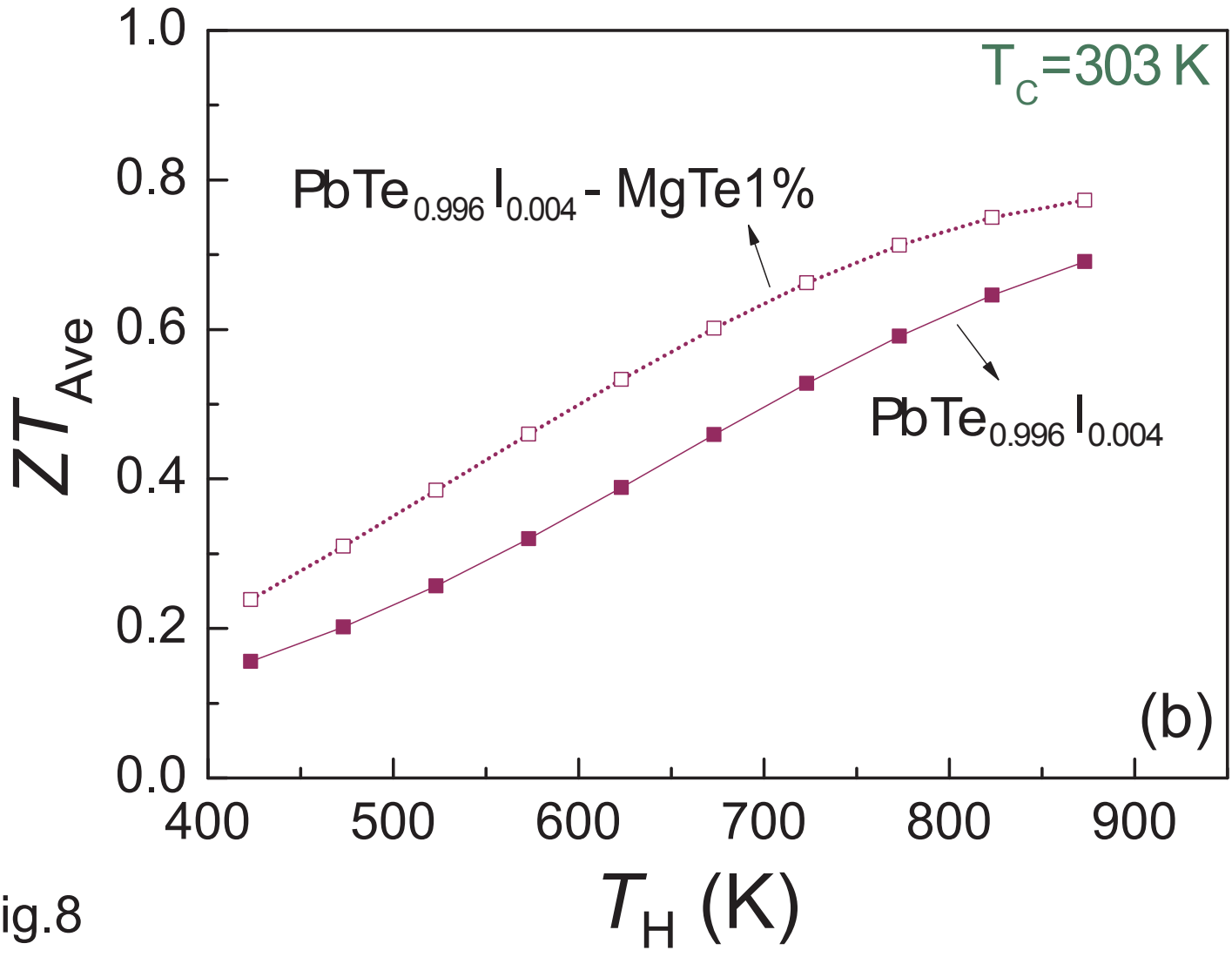

Fig.8